



JAAS

Approach to Using 3D Laser-Induced Breakdown Spectroscopy (LIBS) Data to Explore the Interaction of FLiNaK and FLiBe Molten Salts with Nuclear-Grade Graphite

Journal:	<i>Journal of Analytical Atomic Spectrometry</i>
Manuscript ID	JA-ART-05-2022-000168.R1
Article Type:	Paper
Date Submitted by the Author:	13-Jun-2022
Complete List of Authors:	Myhre, Kristian; Oak Ridge National Laboratory Andrews, Hunter; Oak Ridge National Laboratory Sulejmanovic, Dino; Oak Ridge National Laboratory, Contescu, Cristian; Oak Ridge National Laboratory Keiser, James; Oak Ridge National Laboratory Gallego, Nidia; Oak Ridge National Laboratory

SCHOLARONE™
Manuscripts

ARTICLE

Approach to Using 3D Laser-Induced Breakdown Spectroscopy (LIBS) Data to Explore the Interaction of FLiNaK and FLiBe Molten Salts with Nuclear-Grade Graphite

Received 00th January 20xx,
Accepted 00th January 20xx

DOI: 10.1039/x0xx00000x

Kristian G. Myhre,* Hunter B. Andrews,* Dino Sulejmanovic, Cristian I. Contescu, James R. Keiser, and Nidia C. Gallego*

Nuclear graphite has historically been a key component of many nuclear reactor designs and has emerged as key to numerous advanced nuclear reactor design concepts. Molten salt reactors (MSRs) are one broad group of advanced reactor designs currently being pursued by industry for commercialization. Several MSR designs under consideration use graphitic materials that directly interface with a molten salt, whether it is a fuel salt, coolant salt, or both. Therefore, the interaction of graphite materials with molten salts must be understood. To gain this required understanding, a range of data is needed including porosity, strength, and composition as a function of different salt exposure parameters. A laser-induced breakdown spectroscopy (LIBS) measurement and data analysis methodology was developed to obtain spatially resolved elemental composition information for graphite samples exposed to a molten fluoride salt. Traditional univariate emission line analysis of atomic, ionic, and molecular optical emission signals was coupled via correlation analysis with spectral decomposition of the data using principal component analysis. Elemental depth profiling and elemental mapping were also performed to visualize salt-graphite interactions. LIBS was demonstrated to be useful for measuring key analytes such as fluorine and hydrogen, which are troublesome for other analysis techniques. Evidence for complex behavior was found, thereby demonstrating the usefulness of the developed approach for future systematic studies.

I. Introduction

Molten salts are receiving an increased level of interest for use in advanced nuclear reactor concepts. A growing number of private companies around the world are actively pursuing the commercialization of molten salt reactor (MSR) concepts, which use molten salts as coolants, fissile fuel carriers, or both. A thorough understanding of how materials interact with the molten salts of interest is key to bringing MSR technologies to market. The material-salt interactions must be understood as they relate to the safety basis of a specific MSR design. This includes, but is not necessarily limited to, issues such as source term (e.g., tritium and fission product transport) and behavior under accident scenarios (e.g., production of reactive gases when inadequately cooled). In addition to licensing, the economic viability of MSRs is crucial to their commercial success. One of several ways to improve the economic viability

of MSRs is to increase their useful lifetime, which is largely driven by the lifetime of materials and frequency of repairs.

Graphite is being considered for use in many MSR designs because it can serve as a neutron moderator and is chemically resistant toward many molten salts, especially fluoride salts. From 1965 to 1969, the Molten Salt Reactor Experiment at Oak Ridge National Laboratory (ORNL) demonstrated that graphite could successfully be used in a molten fluoride salt reactor system.¹ Graphite was selected for the experiment because of its low wettability and higher resistance to corrosion compared to known metal alloys for the fluoride salts of interest, which were 7LiF-BeF₂-ZrF₄-UF₄ as the fuel salt and 7LiF-BeF₂ eutectic as the coolant salt.¹ Today, graphite still receives serious consideration for use in advanced MSR designs being developed by industry that use fluoride-containing salts. The interaction of graphite with molten fluoride salts is therefore of high interest.

Laser-induced breakdown spectroscopy (LIBS) was identified as a useful technique for providing spatially resolved chemical composition data for graphite samples exposed to molten fluoride salts. In recent years, many studies have detailed the use of LIBS for elemental depth profiling and mapping.²⁻²⁸ The reader is pointed toward a recent review by Jolivet et al. for more thorough exposition of published LIBS imaging studies.²² The LIBS technique involves irradiation of a sample with an intense, focused beam of light from a pulsed laser source. The power density achieved is typically in excess of 10 GW cm⁻², high enough to induce localized optical breakdown of the target material thereby resulting in the formation of a plasma. Excited species in the plasma, mostly

Oak Ridge National Laboratory, 1 Bethel Valley Rd., Oak Ridge, TN, 37830, USA.

Email: K. Myhre—myhrek@ornl.gov, H. Andrews—andrewshb@ornl.gov,

N. Gallego—gallegonc@ornl.gov

*This manuscript has been authored by UT-Battelle, LLC, under contract DE-AC05-00OR22725 with the US Department of Energy (DOE). The US government retains and the publisher, by accepting the article for publication, acknowledges that the US government retains a nonexclusive, paid-up, irrevocable, world-wide license to publish or reproduce the published form of this manuscript, or allow others to do so, for US government purposes. DOE will provide public access to these results of federally sponsored research in accordance with the DOE Public Access Plan (<http://energy.gov/downloads/doe-public-access-plan>).

neutral and ionic atomic species, de-excite and produce an optical emission spectrum characteristic of the sample's composition. Molecular emission lines, almost always from diatomics, may also be observed depending on the experimental parameters as well as sample composition and properties.

This study aimed to investigate the use of LIBS for exploring the interaction of molten FLiNaK (47:11:42 LiF:NaF:KF) and FLiBe (2:1 LiF:BeF₂) salts with graphite and to develop a data analysis methodology for future salt-graphite interaction studies.²⁹ A significant benefit of using LIBS for these studies was the ability to maintain an inert atmosphere, which prevents moisture and oxygen absorption. Standard emission line intensity analysis and an unsupervised learning approach to data analysis (i.e., principal component analysis [PCA]) were explored, separately and in combination, for evaluating the collected LIBS data.

II. Experimental

Sample Production

Commercially available graphite materials were purchased and machined into parallelepipeds with dimensions of roughly 12.7 × 12.7 × 25 mm. A set of graphite samples were exposed to molten FLiNaK using a custom-built molten salt intrusion system, for which the design and operation is discussed in detail elsewhere.²⁹ Briefly, the molten salt intrusion system was designed to enable tests following the guidance provided in the ASTM D8091-16 procedure addressing impregnation of graphite with molten salt. All graphite samples were air-dried at 110°C for 2 h and then heated to 1,200°C for 12 h under vacuum before the intrusion experiments. The intrusion system is capable of operating under temperatures up to 750°C and pressures up to 10 bar. Argon was used as a cover gas to maintain a specified pressure. The intrusion system enables samples to be immersed in a molten FLiNaK bath and withdrawn prior to cooling to avoid freezing the salt around the samples. The first set of samples analysed in this study were

exposed to molten FLiNaK at 750°C and 7.9 bar for 12 h.²⁹ An additional set of graphite samples was exposed to molten FLiBe at 750°C for 1,000 h in static capsule tests. These initial tests required less Be bearing salts to mitigate health and safety concerns while providing information on the compatibility of FLiBe and alloy materials for future system construction. Additional information on the graphite samples investigated is listed in Table 1. For the remainder of this paper, FLiNaK and FLiBe exposed samples have a K or B prefix, respectively.

Laser-Induced Breakdown Spectroscopy Measurements

The samples that were not exposed to molten salts were maintained in an inert atmosphere only during measurements. The samples exposed to FLiNaK or FLiBe were maintained in an inert atmosphere throughout the entirety of the measurements. This was key to limiting any impurities from reaction with or absorption of atmospheric water or oxygen due to the hygroscopic nature of the residual salts. The exposed samples were loaded into the sealable sample holder (Figure 1) under an argon gas atmosphere within an inert glove box. A block of acrylic was machined with rectangular slots to maintain the samples at the correct distance and facilitate greater repeatability. The loaded sample chamber was then sealed to maintain the integrity of the samples and removed from the inert atmosphere glove box to be loaded into the LIBS instrument chamber. Once mounted onto the three-axis translation stage by set screws, the inlet and outlet gas connections were made. The inlet was connected to a helium compressed gas cylinder. A flow rate of 0.1 L min⁻¹ of helium was used even when no measurements were being performed. The outlet was connected to a JSL series JetStream HEPA filter vacuum system from Quatro Air Technologies. LIBS measurements were performed using a J200-ns LIBS instrument from Applied Spectra. The system included an Nd:YAG laser operating at the fourth harmonic wavelength of 266 nm. The laser energy was 16.4 ± 0.32 mJ. The beam diameter on the sample was 200 µm. The fluence and power density were

Table 1. Characteristics of various graphite samples investigated.

	Sample Tag	Graphite Grade	Grain Size µm	Bulk density g cm ⁻³	Skeleton density g cm ⁻³	Open pores volume cm ³ g ⁻¹	Closed pores volume cm ³ g ⁻¹	Total pores volume cm ³ g ⁻¹	Porosity %	Pore opening diameter µm
FLiNaK	K1	NBG-18	1600	1.86	2.02	0.044	0.048	0.092	17	12
	K2	PCEA	800	1.77	2.00	0.065	0.054	0.119	21	64
	K3	IG-110	10	1.76	2.05	0.079	0.041	0.12	21	3.9
	K4	NBG-25	60	1.81	2.07	0.068	0.038	0.105	19	5.1
	K5	2114	13	1.81	2.08	0.071	0.034	0.105	19	3.5
	K6	ETU-10	15	1.74	2.10	0.098	0.031	0.129	22	3.6
FLiBe	B1	ZXF-5Q	1	1.80	2.12	0.083	0.026	0.109	20	0.5
	B2	AXF-GQ	5	1.73	2.10	0.102	0.030	0.131	23	0.9
	B3	TM	10	1.73	2.10	0.102	0.030	0.132	23	2
	K1	NBG-25	60	1.81	2.07	0.068	0.038	0.105	19	5.1
	B5	IG-110	10	1.76	2.05	0.079	0.041	0.12	21	3.9
	B6	PCEA II	800	1.77	2.00	0.065	0.054	0.119	21	64
	B7	PCEA	800	1.77	2.00	0.065	0.054	0.119	21	64
	B8	2114	13	1.81	2.08	0.071	0.034	0.105	19	3.5



Figure 1. Sealed sample chamber used to maintain an inert atmosphere of either argon or helium during storage and measurements. The sample chamber has two gas connectors, an inlet, and an outlet that allow for gas to be flowed through the chamber.

therefore 52.2 J cm^{-2} and 13.1 GW cm^{-2} , respectively. A repetition rate of 10 Hz was used for the laser during the measurements. The laser was fired orthogonally onto the sample surface through the sample chamber window and the light was collected using a collimating lens at approximately a 30° angle from the laser path. An example picture of a graphite sample's surface before and after LIBS analysis is shown in Figure S1 of the Supporting Information.

Data Analysis and Visualization

Analysis of the collected data was performed using a combination of commercial software packages as well as custom scripts written in Python 3.6.2. Initial data analysis was performed using Clarity version 18.00212 from Applied Spectra. The scikit-learn 0.23.2 Python library was used to perform PCA.³⁰ The results from emission line analysis and PCA were visualized using the Plotly Python library.³¹ The hyperspectral data were randomly split into equal partitions to form training and test data. The Pearson correlation coefficient (PCC) was used for correlation analysis.³² Positive PCC values indicate that the two variables being compared have a positive linear correlation. Negative PCC values indicate that the two variables being compared have a negative linear correlation. The linear correlation between two variables is categorized as small, medium, or large if the magnitude (absolute value) of the PCC value is between 0.1 and 0.3, 0.3 and 0.5, or 0.5 and 1.0, respectively. Note, a PCC value magnitude greater than 1 is not

possible. A PCC value magnitude less than 0.1 is categorized as having no linear correlation.

III. Results and Discussion

Determination of LIBS Measurement Parameters

LIBS measurement parameters should be selected with the specific analytes of interest in mind. A high priority for these measurements was the detection of fluorine. The signal-to-noise ratio for fluorine was therefore used to optimize the LIBS measurement parameters. The detection of fluorine through measurement of an optical emission spectrum is challenging compared to many other elements.^{21,32,33} The strongest emission lines for fluorine are in the vacuum-ultraviolet spectral region (i.e., below 100 nm), thereby requiring specialized detectors and measurement conditions such as vacuum atmospheres.³³ The latter must be maintained along the entire light path from the emission source, in this case the laser-induced plasma, to the detector. A sealed sample chamber filled with an inert gas, either argon or helium, was used in this work to maintain sample integrity. A picture of the chamber loaded with several samples is given in Figure 1. Although the atmospheric conditions of the sample chamber itself can be controlled with the current setup, the entire light path cannot. The emitted photons must go through the chamber window, a few centimeters of ambient air, a collection lens, and a short fiber-optic cable, making meaningful photon detection in the vacuum-ultraviolet spectral region not viable. An alternative is to measure the concentration of fluorine using molecular emission lines, such as those from CaF, for quantitative detection in laser-induced plasmas.³² The molecular emission method requires calcium to be added if not already present in adequate concentration to produce meaningful amounts of CaF. The addition of calcium was determined to be impractical for the type of sample analyzed in this work because of our desire to perform depth profiling, which would require calcium be added in a cover gas or repeatedly to the surface being analyzed. The visible and near-infrared optical emission lines of fluorine are the third option and were used for this work for fluorine detection. Several studies have been published using the visible and near-infrared emission lines, with the main line being the F I line at 685.6 nm.^{21,32,33} Helium atmospheres are the preferred choice for measuring the visible and near-infrared emission lines of F I when performing measurements under vacuum is not practical.^{21,32,33} As noted in previous studies, the delay time is an important factor for detecting the F I emission lines, with delay times of less than $1 \mu\text{s}$ frequently used.^{21,32,33} This is a shorter delay time than typical for lines from C, Na, Li, and K, which are the other elements of interest in this study. The shorter delay time effectively results in measurement of a higher apparent plasma temperature. The calculated intensities for major emission lines from relevant species of C, Be, Na, Li, F, and K as a function of plasma temperature are shown in Figure 2. An increase in temperature first leads to an increase in intensity for the neutral species until ionization occurs at a

significant enough level where the emission intensity decreases. The F I 685.603 nm emission line can be seen to reach maximum intensity just above a plasma temperature of 1.5 eV, which is significantly higher than the other elements. This results from the high electronegativity of fluorine and resulting high excitation energy.

The signal-to-noise ratio of the F I 685.603 nm emission line was used in this study to select the delay time and laser pulse energy. LIBS spectra from 680 to 690 nm of a graphite sample exposed to molten FLiNaK at various energies (100%, 80%, 60%, 40%, and 20% of the maximum 16.4 mJ) and delay times (0.25, 1, 2, 5, and 10 μ s) are shown in Figures S2 and S3 of the Supplementary Information. The variable energy measurements were performed with a delay time of 0.25 μ s. The variable delay time measurements were performed with 100% energy. The highest signal-to-noise ratio for the F I 685.603 nm emission line was achieved with a delay time of 0.25 μ s and laser pulse energy percentage of 100%, as seen in

Figures S2 and S3 of the Supporting Information. These parameters were used for all subsequent LIBS measurements. The same settings were applied to the FLiBe-exposed samples as well due to Be II and F I having similar intensity vs temperature trends.

Hyperspectral imaging data was collected as a function of depth to produce 3D hyperspectral LIBS data. The x-axis and y-axis dimensions consisted of a 10 by 10 grid of analysis spots spaced 250 μ m apart center-to-center. The z-axis dimension consisted of 50 laser shots at a given grid position. The depth per shot was estimated to be \sim 200 nm based on previous depth profiling work,³⁴ although future work should more carefully investigate the ablation rates of graphite samples because they may be dramatically different from metal samples. The hyperspectral data was then segmented using one of two data analysis methods: univariate emission line analysis and PCA.

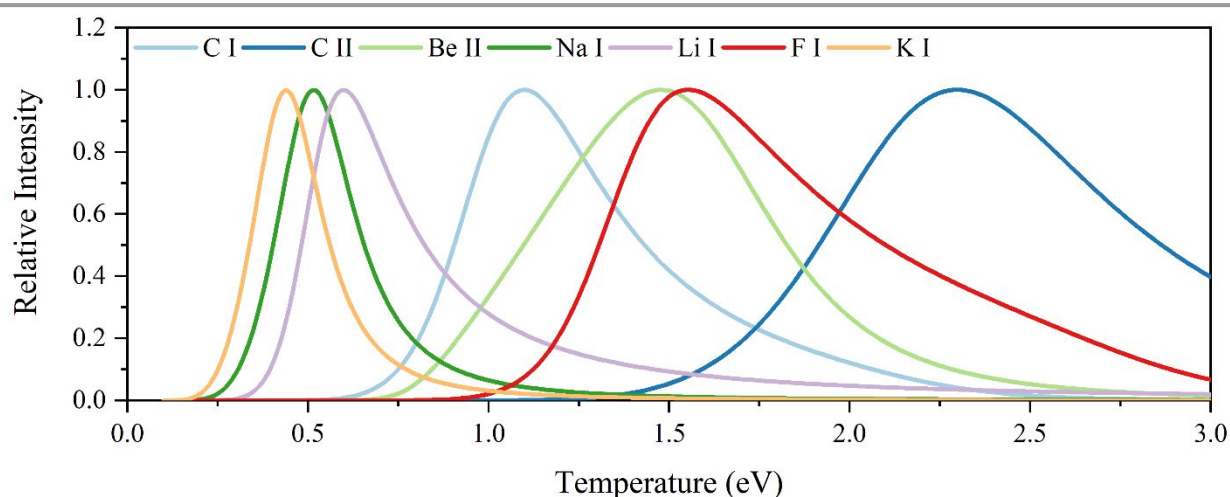


Figure 2. Calculated normalized intensities of select carbon, beryllium, sodium, lithium, fluorine, and potassium emission lines as a function of plasma temperature (eV) using the Saha-Boltzmann relation. The graph illustrates that higher temperatures (more energy) are required to produce similar normalized intensities of neutral species for fluorine as compared to sodium, lithium, potassium, and carbon. Note that the normalized intensities decrease after reaching a maximum due to ionization of neutral species.

Emission Line Analysis

Emission line analysis involves calculation of the signal for an observed emission line. The background-corrected emission line intensities were used as the signal data for univariate analysis. The integrated peak intensity was calculated using the approach described in previous work.^{35,36} Briefly, a simple integration of two spectral regions, an emission line region and a nearby background region where there are no emission peaks, were calculated for each spectrum. The background region was then subtracted from the emission line region. The resulting difference was then divided by the background region, resulting in the final background-corrected and normalized signal used for univariate emission line analysis. The emission lines used for emission line analysis are listed in Table 2, which provides an abbreviated list of all emission lines observed. Figure 3 shows example single-shot spectra of

frozen FLiNaK salt, an unexposed graphite sample, a graphite sample after exposure to molten FLiNaK, and a graphite sample after exposure to molten FLiBe.

Emission lines for neutral and singly ionized carbon species were observed in all of the LIBS spectra; this was expected because the sample matrix was graphite. LIBS analysis of carbon-based materials typically uses longer delay times and lower fluences than the 0.25 μ s delay time and 52.2 J cm⁻² fluence used in this work.^{37,38} Observations related to emission lines from ionized carbon species are not typically reported for this reason. The spectra measured in this work were taken at higher apparent plasma temperatures to optimize for detection of fluorine, as previously mentioned. The plasmas in this work were observed at high enough temperatures for measurable amounts of C II to be produced and excited. Emission lines for

neutral hydrogen, neutral helium, and neutral oxygen were observed in both the graphite samples that were and were not exposed to molten salts. The hydrogen and oxygen were likely predominately present as residual absorbed water and oxygen. Helium was used as the cover gas during LIBS measurements and therefore expected to be observed in every spectrum. Emission lines for F I, Li I, Na I, and K I were observed in the LIBS spectra of the FLiNaK-exposed graphite samples. Emission lines for F I, Li I, and Be II were observed in the LIBS spectra of the FLiBe-exposed graphite samples. No emission lines for ionized fluorine, lithium, or sodium were observed. A frozen piece of the FLiNaK used for the intrusion tests was tested to verify peak identification, peak ratios, and identify impurities. Several additional fluorine and potassium lines were seen in the salt sample. Neutral hydrogen and oxygen lines were identified, confirming the presence of trace moisture in the salt itself.

FLiNaK-Exposed Emission Line Analysis

Correlation analysis was performed to understand the relationship among the univariate emission signals measured. The matrix of PCC values for H I, He I, Li I, C I, O I, F I, Na I, K I, C II, and C₂ Swan in Sample K1 is shown in Table S1 of the Supporting Information with results described here. The Li I, F I, Na I, and K I signals were found to have a large correlation with each other. The large correlation of FLiNaK salt constituent signals is intuitive. The H I signal matrix was found to have a large positive correlation to the O I signal matrix; a small positive correlation to the C II and FLiNaK salt signal matrices; a small negative correlation to the C₂ Swan signal matrix; and no correlation to the He I and C I matrices. The large positive correlation of the H I and O I signal matrices is likely due to hydrogen and oxygen being present in the sample as water. The H I signal had a small positive correlation with the salt signal matrices, but O I only had a small positive correlation with F I. These correlations of hydrogen and oxygen with constituents of FLiNaK are likely due to the absorption of water by the FLiNaK salt, which is very hygroscopic. Water and oxygen absorption will still have occurred despite the samples being kept in an inert environment. The H I is most highly correlated with fluorine- and potassium-related signals across the FLiNaK-exposed samples. This may indicate a preferential absorption of water by a

partitioned KF phase. The C I and C II signal matrices were found to have a high positive correlation, which likely balanced the formation of both species in plasmas of the same temperature with the parasitic relationship of C II formation from C I at higher plasma temperatures. The He I signal matrix did not have any consistent large positive correlations; this can be expected because the He I signal was from the cover gas and not part of the matrix itself. However, the He I signal had a strong negative correlation with most of the salt signal matrices. This can be attributed to a difference in the plasma formation in the presence of FLiNaK, altering the contribution of He to the plasma composition. Interestingly, the C₂ Swan signal has a small negative correlation to the He I signal matrix and a small-to-medium positive correlation to the Li I, Na I, and K I signal matrices. This relationship indicates that the formation, excitation, or a combination of formation and excitation of diatomic carbon in the plasma is related to the presence of FLiNaK. This could be related to the plasma temperature with the presence of FLiNaK salt constituents, especially fluorine, requiring more energy for excitation compared to pure carbon, thereby decreasing the amount of diatomic carbon destroyed during the laser-induced plasma formation process. While minor fluctuations were seen, these results are representative of the entire set of FLiNaK-exposed graphites.

FLiBe-Exposed Emission Line Analysis

The same correlation analysis was performed for the FLiBe-exposed samples using relevant lines. The matrix of PCC values for H I, He I, Li I, C I, O I, F I, Be II, C II, and C₂ Swan in Sample B1 is shown in Table S2 of the Supporting Information with results described here. The He I signal showed large positive correlations with the O I and C II signal matrices, but no major trends were found across all FLiBe-exposed graphites. This indicates the positive correlations found were spurious. The H I signal showed varying levels of positive correlations with the O I signal matrices and low negative correlations to salt signal matrices. Here, Sample B1 differed from the other FLiBe-exposed samples which showed small-to-medium positive

Table 2. Abbreviated list of atomic, ionic, and molecular emission lines identified in this work. The emission lines in this table were used for univariate emission line analysis.

Species	Observed wavelength (nm)	NIST wavelength ⁴¹ (nm)
H I	656.26	656.279
He I	706.667	706.519
Li I	610.333	610.353 610.365
C I	247.818	247.856
O I	777.35	777.194 777.417 777.539
F I	685.619	685.603
Na I	588.975	588.995
K I	766.479	766.49
Be II	313.026	313.042 313.107
C II	283.705	283.672 283.761
C ₂ Swan	516.435	Ref. 42

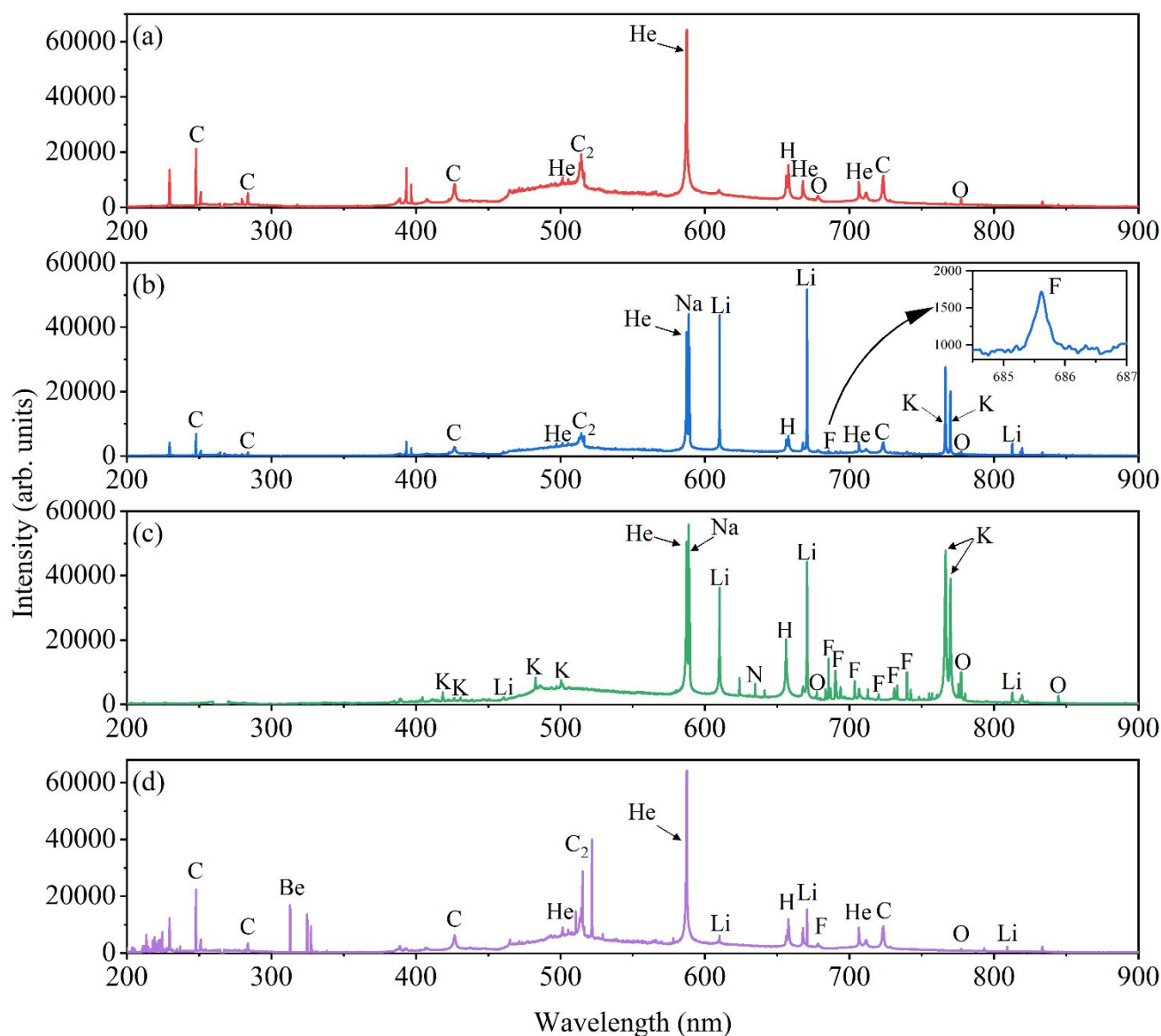


Figure 3. Collected surface spectra of (a) unexposed graphite, (b) FLiNaK-exposed graphite (Sample K1), (c) frozen FLiNaK salt, and (d) FLiBe-exposed graphite (Sample B5). All samples were collected under a He cover gas with the same acquisition settings. The laser line at 266 nm was removed from spectra prior to analysis.

correlations between the H I and salt signal matrices. This may indicate FLiBe is less affected by absorption of water than FLiNaK, though further studies would be required to draw conclusions. The H I signal also showed medium-to-high positive correlations with carbon emissions, particularly the C2 Swan signal. As expected, the FLiBe salt constituents show large positive correlations with one another. The salt emission peaks show varying levels of correlation to C I, C II, and C2 Swan emissions with no clear trends seen throughout the sample set. This lack of correlation is likely due to the absence of external pressure forcing the intrusion of FLiBe salt into the graphite pores. The C I, C II, and C2 Swan signals were all positively correlated, exhibiting the same behavior as the FLiNaK data.

Spectral Dimensionality Reduction with PCA

PCA, an unsupervised learning approach, was used for spectral decomposition of the LIBS depth profiling data with the goal of increasing interpretability through dimensionality reduction. The goal of PCA is to optimally describe the variance in the spectral data by projecting the original data onto a new latent variable space with reduced dimensionality.³⁹ Detailed analysis of the first five principal components for PCA was completed for FLiNaK- and FLiBe-exposed samples, respectively.

FLiNaK PCA Investigation

Generally, the first five components, PCA-C1 through PCA-C5, were seemingly most appropriate to describe the variability of FLiNaK-exposed graphite data while maintaining a reasonable number of components with physical meaning. PCA-C6 through

PCA-C10 each explain 1.5% or less of the spectral variance. Although PCA-C6 through PCA-C10 have well-defined spectral loadings, they do not show any large correlations to the signal matrices determined through univariate emission line analysis. Correlation analysis between the 3D univariate emission line data and the PCA scores was performed to better understand the meaning behind each PCA component. The resulting PCC values for Sample K1 are provided in Table 3 and discussed below.

PCA-C1 explains 81.5% of the spectral variance in Sample K1's spectra. The PCA-C1 scores matrix has a large positive correlation to the Li I, F I, Na I, and K I signal matrices; a small positive correlation with H I and C2 Swan signal matrices; a small negative correlation with the C II signal matrix; and a large negative correlation with He I and C I signal matrices. The species that PCA-C1 is positively correlated with are components of FLiNaK. The PCA-C1 loading vector, shown in Figure S4 in the Supporting Information, shows positive loading coefficients for emission lines associated with Li I, F I, Na I, and K I. PCA-C1 is also positively correlated with the formation of diatomic carbon species, which may indicate that diatomic carbon forms more readily with increased FLiNaK content. This was also indicated during the previously discussed emission signal correlation analysis. The species that PCA-C1 is negatively correlated with are related to graphite. PCA-C1 can therefore be categorized as showing the distribution of FLiNaK vs. graphite with the ratio of FLiNaK to graphite, increasing with the score of PCA-C1.

PCA-C2 explains 7.3% of the spectral variance for Sample K1, a significant decrease from its predecessor. The PCA-C2 score matrix has no large correlations with any species. PCA-C2 has small positive correlations with Li I, O I, Na I, K I, and C2 Swan signal matrices and low negative correlations with H I, He I, C I, and C II signal matrices. Inspection of the loadings for PCA-C2 provides further information. The PCA-C2 loading vector is negative for carbon species and helium, indicating that PCC values should be interpreted in reverse. In short, PCA-C2 is a score of the purity of the graphite.

PCA-C3 explains 4.1% of the spectral variance for Sample K1. The PCA-C3 score matrix has a small positive correlation to the F I signal matrix; a small negative correlation to the H I, C I, and Na I signal matrices; and a medium negative correlation to the He I and C2 Swan signal matrices. The PCA-C3 loading vector shows negative coefficients for carbon species and the He I signal. The loadings for other species' peaks are negative, but the peak shoulders are given positive coefficients. PCA-C3 is likely a score of the spectral background due to mostly graphite concentration. Thus, the majority of spectral variance is explained by the overall sample concentration (or density). Future work could measure the total ablated mass in addition to the LIBS spectrum for each analysed spot to better understand the nature of PCA-C3. Previous work by Prochazka et al.⁴⁰ exhibited similar matrix effects that were explained by the first component during PCA of LIBS data of bacteria.

PCA-C4 explains 2.8% of the spectral variance. The PCA-C4 score matrix shows a large positive correlation to the He I signal matrix; a medium positive correlation to the F I signal matrix;

and small positive correlations with C I, O I, and K I signal matrices. The loading vector shows a positive coefficient for the He I and F I signals and positive coefficients for the K I and O I signal baselines. This leads to PCA-C4 likely accounting for further background effects.

PCA-C5 explains 1.6% of the spectral variance. The score matrix shows a large positive correlation to the C2 Swan signal matrix; a small positive correlation to the C I, F I, and K I signal matrices; and a small negative correlation to the He I, Li I, and O I signal matrices. The loading vector shows a positive coefficient assigned to the carbon molecular band as well as the K emission peaks. The coefficient for the 610.35 nm Li I line is negative, and the coefficient for the 670.77 nm Li I line is positive. This can be interpreted as Li having no major effect on PCA-C5. Rather, the component seems to focus on the diatomic carbon and potassium emissions.

The PCA analysis was completed in the same fashion for the remaining FLiNaK-exposed samples with similar results. The first three components typically captured the major relationships pertaining to the salt signal, the graphite signal, and the background/matrix effects. Moisture relationships were typically captured in either the salt or graphite principal components. The latter two components mostly captured helium, diatomic carbon, or remaining background variance.

FLiBe PCA Investigation

As with the FLiNaK-exposed graphite data, the first five PCA components generally offer the most useful explanation of the spectra variance. PCA components beyond five were investigated but typically explained less than 1.5% of the spectral variance making their physical explanation less evident. The resulting PCC values for Sample B1 are provided in Table 4 and discussed below.

PCA-C1 explains 81.3% of Sample B1's spectral variance. The PCA-C1 score matrix has a large positive correlation to the H I, He I, C I, and C II signal matrices; a medium positive correlation to the C2 Swan signal matrix; a small positive correlation to the O I signal matrix; and small negative correlations to the Li I and Be II signal matrices. The PCA-C1 loading vector, shown in Figure S5 in the Supporting Information, shows negative coefficients for all emission signals, except for Li I. PCA-C1 is therefore related to the inverse of the graphite purity. As the salt present decreases and the carbon peaks become more intense, the PCA-C1 score decreases.

PCA-C2 explains 6.4% of Sample B1's spectral variance. PCA-C2 shows a large positive correlation to Li I, F I, and Be II signal matrices; a small negative correlation to the He I signal matrix; and a medium negative correlation to the H I and C2 Swan signal matrices. The PCA-C2 loading vector shows a positive coefficient for carbon and salt species and a negative coefficient for the helium line. The largest weighted signal is that of the Be II line. This leads to PCA-C2 being attributed to the signal variance from salt species. The negative correlation to the C2 Swan emission may indicate that the diatomic carbon emission is less likely in the presence of FLiBe. This is different from the behavior observed with FLiNaK, but the difference could also be

due to FLiBe being only a surface-level contaminant, whereas FLiNaK samples had intrusion. Another interesting finding is

Table 3. Correlation analysis between the 3D distributions of elements and the principal components from PCA for Sample K1.

	Explained variance	H I	He I	Li I	C I	O I	F I	Na I	K I	C II	C ₂ Swan
PCA-C1	81.5%	0.15	-0.54	0.95	-0.48	0.01	0.73	0.92	0.91	-0.14	0.21
PCA-C2	7.3%	-0.28	-0.24	0.18	-0.19	0.1	-0.08	0.23	0.11	-0.29	0.13
PCA-C3	4.1%	-0.23	-0.32	-0.09	-0.3	-0.05	0.25	-0.28	-0.09	-0.12	-0.34
PCA-C4	2.8%	0.05	0.64	0.02	0.18	0.2	0.32	-0.06	0.14	-0.01	0.02
PCA-C5	1.6%	0.02	-0.23	-0.17	0.18	-0.21	0.1	-0.01	0.23	0.09	0.54

Table 4. Correlation analysis between the 3D distributions of elements and the principal components from PCA for Sample B1.

	Explained variance	H I	He I	Li I	C I	O I	F I	Be II	C II	C ₂ Swan
PCA-C1	81.3%	0.53	0.67	-0.28	0.61	0.29	-0.09	-0.19	0.91	0.41
PCA-C2	6.4%	-0.32	-0.15	0.62	-0.05	-0.09	0.7	0.86	-0.04	-0.35
PCA-C3	4.5%	0.41	0.02	0.16	0.25	0.14	-0.01	0.02	0.22	0.63
PCA-C4	2.3%	0.08	-0.37	-0.54	0.26	-0.29	-0.37	0.04	0.16	0.15
PCA-C5	1.5%	0.46	-0.47	0.27	-0.08	-0.05	0.13	0.08	-0.02	0.4

that the hydrogen and oxygen emissions are more captured in the graphite purity component (PCA-C1) than in the salt component (PCA-C2). This adds weight to the observation in the emission peak correlation analysis that FLiBe salts appear less affected by moisture absorption than FLiNaK.

PCA-C3 explains 4.5% of Sample B1's spectral variance. PCA-C3 had a large positive correlation to the C2 Swan emission signal matrix; a medium positive correlation to H I signal matrix; and a small positive correlation to Li I, C I, O I, and C II signal matrices. The PCA-C3 loadings show negative coefficients for salt species and positive coefficients for carbon species and the H I emission signal. This component again shows a correlation between the H I and C2 Swan band. The H I emission peak is highly affected by plasma conditions, as the peak is typically used to determine plasma density. The formation of diatomic carbon in the plasma depends highly on these conditions; thus, this component may capture variance in the plasma properties.

PCA-C4 explains 2.3% of Sample B1's spectral variance. This component had a small positive correlation to the C I, C II, and C2 Swan signal matrices; a small negative correlation to the O I signal matrix; a medium negative correlation to the He I and F I signal matrices; and a large negative correlation to the Li I signal matrix. Investigation of the loadings show positive coefficients for most of the spectra; however, the C2 Swan band background region and the He I peak shoulders have negative coefficients.

PCA-C5 explains 1.5% of Sample B1's spectral variance. PCA-C5 shows a medium positive correlation to the H I and C2 Swan signal matrices; a small positive correlation to the Li I and F I signal matrices; and a medium negative correlation to the He I signal. The loading vector shows positive coefficients for all signals except the He I and Li I peaks. Both PCA-C4 and PCA-C5

appear to capture variance in the background signals. This can be inferred from the loading vectors weighing peak shoulders and centroids differently and also the broad features in the loadings. Due to the FLiBe salt being a surface-level contaminant rather than a penetrated component, there was likely a larger variance in the background emissions while boring into the graphite with sequential shots.

As with the FLiNaK samples, most of the FLiBe PCA results provided similar findings. These components typically could be attributed to the salt, moisture, graphite, or some combination of these signals. The latter PCA components were generally related to background effects or perhaps captured variance in the plasma properties. The PCA provides an additional factor for identifying and validating the relationships seen in the emission peak correlation analysis. These PCA components can also be mapped over the sample surface or used to build depth profiles and examine how the overall salt signal varies spatially. However, in this study, only the emission peak depth profiles and maps will be discussed, as they are more convenient for comparing amongst different samples.

Elemental Depth Profiling and Mapping

The values calculated during the emission line analysis were also investigated as a function of shot penetration. A 10 × 10 shot pattern was used to scan each sample. Each spot was shot sequentially up to 200 times, but only the first 50 shots were used. Data collected from shots above 50 showed no significant salt emission signals. The emission signals as a function of shot number for the FLiNaK-exposed graphites are shown in Figure 4. Each emission line y-scale was mean-centered and only the first 25 shots were plotted to better see the salt penetration

near the surface and compare differences between the graphite samples.

H I and O I signals are much greater at the surface of the samples and show a penetration level of approximately five shots. The F I, Li I, Na I, and K I signal trends match for their respective samples. This may indicate that the bulk salt penetration is representative of the FLiNaK salt composition and that any partitioning, such as a KF component, would exist on a much lower level. The F I emission signal depth profiles generally show a lower level of penetration than the other salt components, although this is likely due to the F I signal being significantly weaker than the others. The salt species seem to

show a penetration level around five shots, corresponding to moisture.

Samples K1 and K2 differ from the other salt penetration trends, showing significantly higher surface levels and a greater penetration range. These two graphite grades have larger grain size, and their pore diameters are quite different from the others, as detailed in Table 1. This increase in average surface-level salt concentration can be attributed to those differences. The apparent increased penetration depth is likely an artifact of the greater surface levels, rather than a significant difference from other graphite grades. This is supported by weight gain during the FLiNaK intrusion tests, which showed Samples K1 and K2 to have the lowest intrusion volumes.²⁹

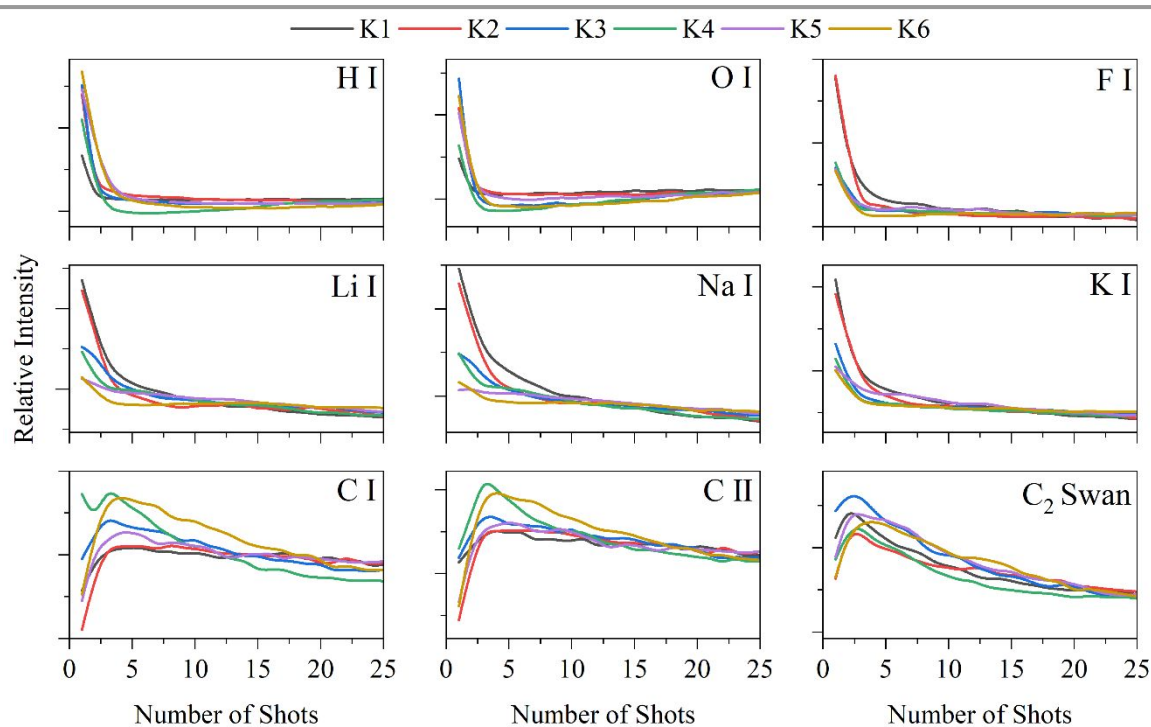


Figure 4. Emission line depth profiles for FLiNaK-exposed graphite samples. The y-scale for each trend has been mean-centered for better qualitative comparison between samples.

The carbon emission signals increase as salt emission signals decrease. Interestingly, the salt-to-carbon ratios decrease as salt emission signals decrease. This appears to be consistent for different salt species for a given sample. In other words, the Li/C ratio decreases at the same rate as the Na/C ratio decreases for sample K1. This represents the ratio change from salt to graphite and shows a consistent salt composition. The C2 Swan emission signal reaches a maximum value slightly faster than C I and C II (~2 vs 4 shots). This complements the earlier hypothesis that the C2 Swan band forms much more readily when salt is present, but at the outermost surface the increased salt levels may mitigate this behavior. This explanation matches the salt species' and the C2 Swan band having small-to-medium positive correlations, rather than large. A slight slope can be seen in most trends beyond 10 shots; although it is more apparent in the carbon emission trends, this is likely due to the optical configuration of the LIBS experiment being altered as the graphite sample surface was ablated further from the optimal focal point with

each successive shot. The difference between the C I, C II, and C2 Swan emissions may also be related to this changing depth phenomenon. Future studies could systematically investigate signal vs shot depth of a more homogenous material to determine the underlying relations.

While the depth profiles show averaged behavior of the salt species' penetration into the graphite, layered 2D maps were also constructed to examine location-specific behavior. The 2D emission signal maps of Sample K1 for C I, F I, Li I, Na I, and K I signals are shown in Figure 5. The first, third, sixth, ninth, and twelfth shot depth layers are mapped to visualize the decay of salt species emissions; meanwhile the carbon signal remains relatively unchanged. Regions can be seen in the maps where the salt is gathered, likely coincident with a large pore. The Li I and Na I signals provide the best examination of salt locations within the graphite sample given their more intense signals. Three hot spots correspond to salt accumulation. The first hot spot (21.2 mm, 71.4 mm) shows F I intrusion up to six shots and Li I and Na I

intrusion up to approximately nine shots. The second hot spot's signal (22.7 mm, 71.1 mm) for all salt species throughout the 12 shots shown in Figure 5. Additionally, the absence of carbon in this spot can be seen in the C I maps. The third hot spot (22.7 mm, 71.6 mm) appears to be mostly at the surface, diminishing after three shots. These maps illustrate that the increased salt species' penetration seen in the depth profiles shown in Figure 4 is indeed due to the sample's increased pore diameter, rather than a systematic greater level of intrusion.

The same depth profile analysis was performed for the FLiBe-exposed samples; due to the lack of external pressure applied during the exposure, no significant penetration trends were observed. This confirms that the FLiBe-exposed samples in this study exhibit only surface-level interactions. Future testing will involve using the salt intrusion system briefly described earlier with FLiBe salts to better understand graphite–FLiBe interactions.

2D emission signal maps were constructed for the carbon and salt species' surface levels on Sample B1 (Figure 6). There are several notable features in the maps. First, the carbon emission

singles are more intense on the left side of the sample and steadily decrease as the sample is scanned to the right. This could be an artifact of the sample surface being slightly tilted relative to the translation-stage plane, or more simply the salt layer on the sample surface may have been uneven in this sample. This effect is mitigated in sequential shots, but in the case of the FLiBe-exposed samples, the surface is of most interest. Second, five cold spots appear along the diagonal of the sample surface where the signal from all species is significantly lower. This likely corresponds to a feature in the graphite surface, such as pits or large pores, that impacted the ablation process, thereby reducing the signal relative to other locations. Lastly, the salt accumulation can be seen in the upper right portion of the sample surface where F I, Li I, and Be II levels are the greatest. This is a great example of how LIBS can provide an elemental map including fluorine and beryllium levels in an inert environment. This capability is crucial for molten salt research where inert atmospheres are vital, impurities have large impacts, and toxic elements are frequently at use.

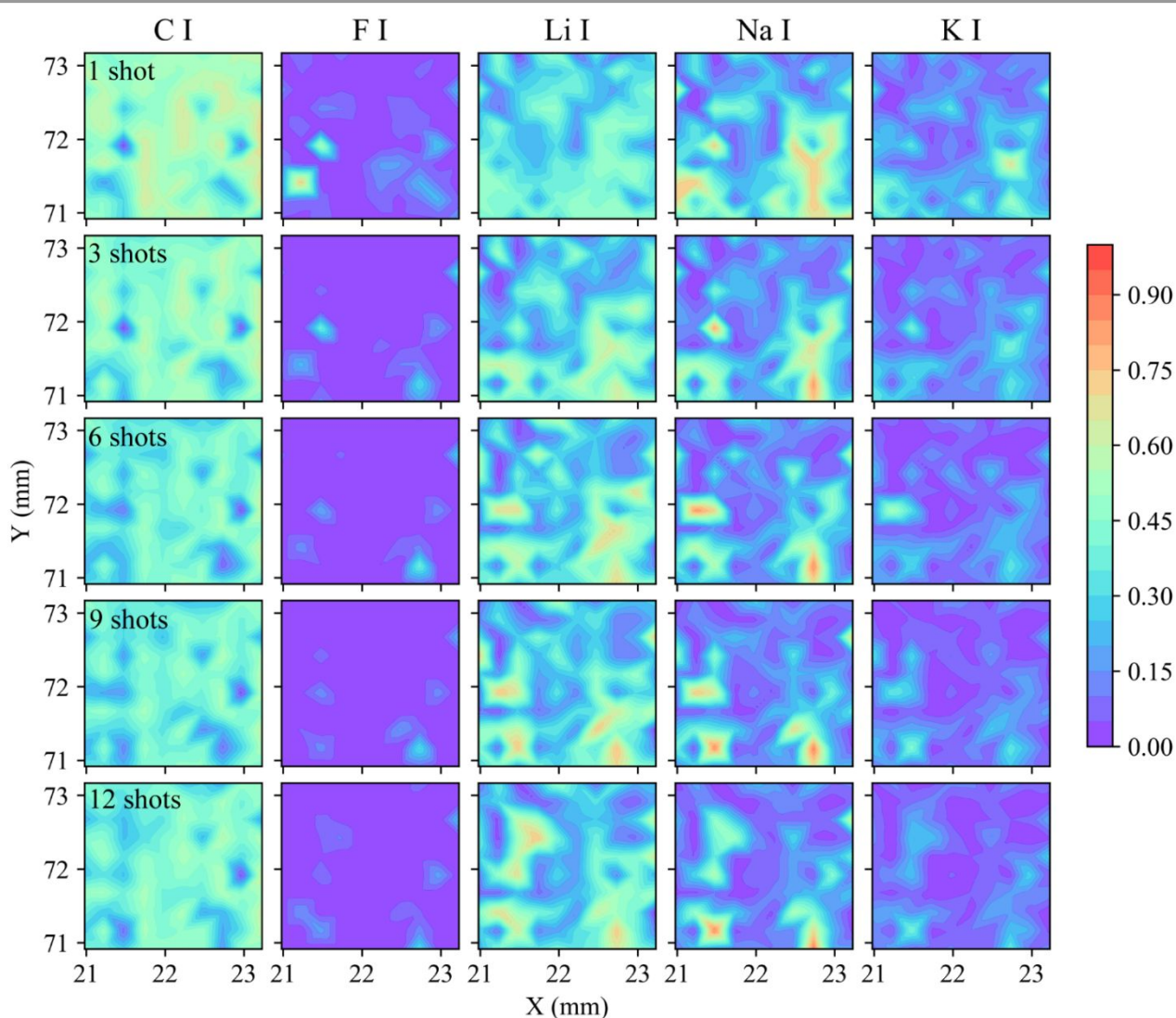


Figure 5. Normalized species' emission peaks mapped over sampling area for Sample K1. Columns show descending shot layers into the sample surface.

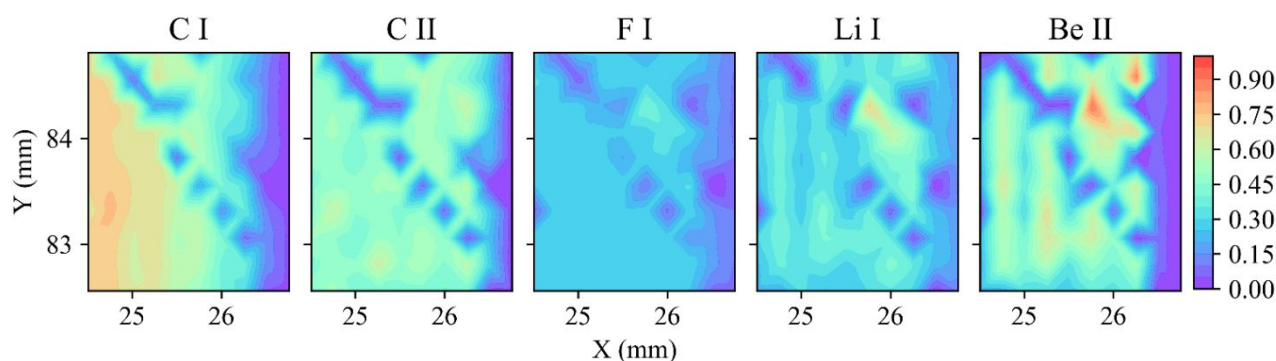


Figure 6. Normalized species' emission peaks mapped over sampling area for Sample B1. No depth analysis was performed due to exposure tests not applying external pressures.

Conclusions

This study showed LIBS to be a useful tool for exploring the interaction of molten salts with nuclear-grade graphite. Depth profiles of H, Li, C, O, F, Na, and K in a graphite matrix were obtained using univariate analysis of known emission lines for neutral species. Emission line analysis was also performed for singly ionized beryllium, carbon, and diatomic carbon (C₂ Swan). PCA was used to better understand the interaction of molten FLiNaK and FLiBe with graphite. Correlation analysis was performed on the spatially resolved univariate emission signals and the first five principal component scores from PCA. The correlation analysis was helpful in interpreting the PCA results, which revealed a more complex behaviour than originally expected. 3D distribution of FLiNaK in the porous graphite matrix was found to be inhomogeneous. Analysis of the 3D spectral data was found to provide more detailed information compared to conventional depth profile analysis. The 2D surface mapping of FLiBe salt on graphite surfaces also demonstrates the feasibility of extending 3D analysis to future FLiBe intrusion tests. The results from this study suggest that a reaction between the FLiNaK and graphite may occur and involve the partitioning of KF from the bulk FLiNaK, albeit at a low level. However, the purpose of this study was not to understand the reactions taking place but rather to develop a methodology for acquiring and analyzing 3D hyperspectral data of graphite samples exposed to molten fluoride salts. Future work will investigate the chemical reactions taking place through systematic examination with LIBS of a large sample set of FLiNaK-exposed graphite samples. This large sample set will likely need to include samples exposed to salts for different times and at different pressures to identify with certainty those characteristics belonging to specific graphite grades. Fortunately, LIBS is very amenable to high throughput testing to enable these large systematic studies in the future.

A positive correlation between carbon and fluorine signals was not seen in any FLiNaK- or FLiBe-exposed graphites. If any carbon-graphite chemical reactions did occur, they were too minor to be identified with LIBS. Additional techniques, such as Raman spectroscopy, may also be useful for confirming the presence of fluorocarbon bonds in the samples. This study has

laid the foundation for ongoing efforts to systematically study the interaction of molten salts with materials, such as graphite and metal alloys. The use of additional approaches to complement univariate emission analysis and PCA should also be explored and may even be helpful in revealing new material behavior(s).

Author Contributions

Kristian Myhre – *Conceptualization, Data curation, Formal Analysis, Funding acquisition, Investigation, Methodology, Visualization, Writing – original draft, Writing – review & editing*, Hunter Andrews – *Formal Analysis, Investigation, Software, Visualization, Writing – original draft, Writing – review & editing*, Dino Sulejmanovic – *Investigation, Resources*, Cristian Contescu – *Conceptualization, Supervision, Writing – review & editing*, James Keiser – *Conceptualization, Supervision, Writing – review & editing*, Nidia Gallego – *Conceptualization, Funding acquisition, Investigation, Project administration, Resources, Supervision, Writing – review & editing*

Conflicts of interest

There are no conflicts to declare.

Acknowledgements

This work was funded by the US Department of Energy, Office of Nuclear Energy's Advanced Reactor Development Program.

References

- 1 R.C. Robertson. MSRE Design and Operations Report: Part I: Description of Reactor Design. Oak Ridge National Laboratory (ORNL). 1965.
- 2 V. Motto-Ros, V. Gardette, L. Sancey, M. Leprince, D. Genty, S. Roux, et al. "LIBS-based Imaging: Recent Advances and Future Directions". *Spectroscopy*. Advanstar Communications Inc., 2020. 35(2): 34–40.
- 3 C.J.M. Lawley, A.M. Somers, B.A. Kjarsgaard. "Rapid Geochemical Imaging of Rocks and Minerals with Handheld Laser Induced Breakdown Spectroscopy (LIBS)". *J.*

- Geochemical Explor. Elsevier B.V., 2020. 106694. 10.1016/j.gexplo.2020.106694.
- 4 T.O. Nagy, U. Pacher, H. Pöhl, W. Kautek. "Atomic Emission Stratigraphy by Laser-induced Plasma Spectroscopy: Quantitative Depth Profiling of Metal Thin Film Systems". Appl. Surf. Sci. Elsevier B.V., 2014. 302(October): 189–193. 10.1016/j.apsusc.2014.01.125.
- 5 J.R. Chirinos, D.D. Oropeza, J.J. Gonzalez, H. Hou, M. Morey, V. Zorba, et al. "Simultaneous 3-dimensional Elemental Imaging with LIBS and LA-ICP-MS". J. Anal. At. Spectrom. 2014. 29(7): 1292–1298. 10.1039/C4JA00066H.
- 6 B. Busser, S. Moncayo, J.-L. Coll, L. Sancey, V. Motto-Ros. "Elemental Imaging Using Laser-induced Breakdown Spectroscopy: A New and Promising Approach for Biological and Medical Applications". Coord. Chem. Rev. 2018. 358: 70–79. 10.1016/j.ccr.2017.12.006.
- 7 M. Imran, L.-Y. Sun, P. Liu, H. Sattar, D. Zhao, Z. Mu, et al. "Depth Profiling of Tungsten Coating Layer on CuCrZr Alloy Using LIBS Approach". Surf. Interface Anal. 2019. 51(2): 210–218. 10.1002/sia.6569.
- 8 Y. Li, C. Ke, X. Liu, F. Gou, X. Duan, Y. Zhao. "Analysis Liquid Lithium Corrosion Resistance of Er₂O₃ Coating Revealed by LIBS Technique". Fusion Eng. Des. Elsevier, 2018. 136(September 2017): 1640–1646. 10.1016/j.fusengdes.2018.07.001.
- 9 S. Messaoud Aberkane, M. Abdelhamid, K. Yahiaoui, C. Mahieddoune, S. Abdelli-Messaci, M.A. Harith. "Depth Profiling of Alumina Thin Films Using Laser Induced Breakdown Spectroscopy: Structural and Morphological Dependence". Thin Solid Films. Elsevier, 2018. 653(March): 293–300. 10.1016/j.tsf.2018.03.052.
- 10 E. Paulis, U. Pacher, M.J.J. Weimerskirch, T.O. Nagy, W. Kautek. "Investigation of the Wavelength Dependence of Laser Stratigraphy on Cu and Ni Coatings using LIBS Compared to a Pure Thermal Ablation Model". Appl. Phys. A. Springer Berlin Heidelberg, 2017. 123(12): 790. 10.1007/s00339-017-1382-7.
- 11 Y. Li, C. Ke, X. Liu, F. Gou, X. Duan, Y. Zhao. "Compositional Depth Profiles of the Type 316 Stainless Steel Undergone the Corrosion in Liquid Lithium Using Laser-induced Breakdown Spectroscopy". J. Nucl. Mater. Elsevier B.V., 2017. 497: 1–9. 10.1016/j.jnucmat.2017.06.025.
- 12 R. Cerrato, A. Casal, M.P. Mateo, G. Nicolas. "Dealloying Evidence on Corroded Brass by Laser-induced Breakdown Spectroscopy Mapping and Depth Profiling Measurements". Spectrochim. Acta Part B At. Spectrosc. Elsevier B.V., 2017. 130: 1–6. 10.1016/j.sab.2016.11.006.
- 13 C. Pan, X. Du, N. An, Q. Zeng, S. Wang, Q. Wang. "Quantitative Analysis of Carbon Steel with Multi-Line Internal Standard Calibration Method Using Laser-Induced Breakdown Spectroscopy". Appl. Spectrosc. 2016. 70(4): 702–708. 10.1177/00037028166631313.
- 14 J.P. Smith, L. Zou, Y. Liu, X. Bu. "Investigation of Minor Elemental Species within Tablets Using in situ Depth Profiling via Laser-induced Breakdown Spectroscopy Hyperspectral Imaging". Spectrochim. Acta Part B At. Spectrosc. Elsevier B.V., 2020. 165: 105769. 10.1016/j.sab.2020.105769.
- 15 J. Agresti, S. Siano. "Depth-dependent Calibration for Quantitative Elemental Depth Profiling of Copper Alloys Using Laser-induced Plasma Spectroscopy". Appl. Phys. A. 2014. 117(1): 217–221. 10.1007/s00339-014-8363-x.
- 16 J.-H. In, C.-K. Kim, S.-H. Lee, J.-H. Choi, S. Jeong. "Rapid Quantitative Analysis of Elemental Composition and Depth Profile of Cu(In,Ga)Se₂ Thin Solar Cell Film Using Laser-induced Breakdown Spectroscopy". Thin Solid Films. 2015. 579: 89–94. 10.1016/j.tsf.2015.02.061.
- 17 R. Glaus, D.W. Hahn. "Fiber-coupled Laser-induced Breakdown and Raman Spectroscopy for Flexible Sample Characterization with Depth Profiling Capabilities". Spectrochim. Acta Part B At. Spectrosc. 2014. 100: 116–122. 10.1016/j.sab.2014.06.026.
- 18 P. Paris, M. Aints, A. Hakola, M. Kiisk, J. Kolehmainen, M. Laan, et al. "Determination of Elemental Depth Profiles by Multi-spot Averaging Technique of LIBS Spectra". Fusion Eng. Des. Elsevier B.V., 2011. 86(6–8): 1125–1128. 10.1016/j.fusengdes.2011.01.117.
- 19 M.P. Mateo, G. Nicolas, V. Piñon, A. Yañez. "Improvements in Depth-profiling of Thick Samples by Laser-induced Breakdown Spectroscopy Using Linear Correlation". Surf. Interface Anal. 2006. 38(5): 941–948. 10.1002/sia.2352.
- 20 T. Canel, P. Demir, E. Kacar, B. Genc Oztoprak, E. Akman, M. Gunes, et al. "Optimization of Parameters for Depth Resolution of Galvanized Steel by LIBS Technique". Opt. Laser Technol. Elsevier, 2013. 54: 257–264. 10.1016/j.optlastec.2013.06.004.
- 21 C.D. Quarles, J.J. Gonzalez, L.J. East, J.H. Yoo, M. Morey, R.E. Russo. "Fluorine Analysis Using Laser Induced Breakdown Spectroscopy (LIBS)". J. Anal. At. Spectrom. 2014. 29(7): 1238–1242. 10.1039/c4ja00061g.
- 22 L. Jolivet, M. Leprince, S. Moncayo, L. Sorbier, C.-P. Lienemann, V. Motto-Ros. "Review of the Recent Advances and Applications of LIBS-based Imaging". Spectrochim. Acta Part B At. Spectrosc. Elsevier, 2019. 151(October 2018): 41–53. 10.1016/j.sab.2018.11.008.
- 23 V. Motto-Ros, S. Moncayo, F. Trichard, F. Pelascini. "Investigation of Signal Extraction in the Frame of Laser Induced Breakdown Spectroscopy Imaging". Spectrochim. Acta Part B At. Spectrosc. Elsevier B.V., 2019. 155: 127–133. 10.1016/j.sab.2019.04.004.
- 24 F. Gervais, K. Rifai, P. Plamondon, L. Özcan, F. Doucet, F. Vidal. "Compositional Tomography of a Gold-bearing Sample by Laser-induced Breakdown Spectroscopy". Terra Nov. Blackwell Publishing Ltd, 2019. 31(5): 479–484. 10.1111/ter.12417.
- 25 K. Rifai, F. Doucet, L. Özcan, F. Vidal. "LIBS Core Imaging at kHz Speed: Paving the Way for Real-time Geochemical Applications". Spectrochim. Acta Part B At. Spectrosc. Elsevier B.V., 2018. 150: 43–48. 10.1016/j.sab.2018.10.007.
- 26 S. Pagnotta, M. Lezzerini, B. Campanella, G. Gallelo, E. Grifoni, S. Legnaioli, et al. "Fast Quantitative Elemental Mapping of Highly Inhomogeneous Materials by micro-Laser-Induced Breakdown Spectroscopy". Spectrochim. Acta Part B At. Spectrosc. Elsevier B.V., 2018. 146: 9–15. 10.1016/j.sab.2018.04.018.
- 27 S. Pagnotta, M. Lezzerini, L. Ripoll-Seguer, M. Hidalgo, E. Grifoni, S. Legnaioli, et al. "Micro-Laser-Induced Breakdown Spectroscopy (Micro-LIBS) Study on Ancient Roman Mortars". Appl. Spectrosc. 2017. 71(4): 721–727. 10.1177/0003702817695289.
- 28 Y. Gimenez, B. Busser, F. Trichard, A. Kulesza, J.M. Laurent, V. Zaun, et al. "3D Imaging of Nanoparticle Distribution in Biological Tissue by Laser-Induced Breakdown Spectroscopy". Sci. Rep. 2016. 10.1038/srep29936.
- 29 N. Gallego, C. Contescu, J. Keiser. Progress Report on Graphite-Salt Intrusion Studies. Oak Ridge, TN (United States), 2020. 10.2172/1651304.
- 30 F. Pedregosa, G. Varoquaux, A. Gramfort, V. Michel, B. Thirion, O. Grisel, et al. "Scikit-learn: Machine Learning in Python". J. Mach. Learn. Res. 2011. 12(85): 2825–2830.
- 31 P.T. Inc. plotly. Montreal, QC, 2015.
- 32 P. Pořizka, S. Kaski, A. Hrdlička, P. Modlitbová, L. Sládková, H. Häkkinen, et al. "Detection of Fluorine Using Laser-induced Breakdown Spectroscopy and Raman Spectroscopy". J. Anal. At. Spectrom. 2017. 32(10): 1966–1974. 10.1039/C7JA00200A.

- 33 D.A. Cremers, L.J. Radziemski. "Detection of Chlorine and Fluorine in Air by Laser-Induced Breakdown Spectrometry". *Anal. Chem.* 1983. 55(8): 1252–1256. 10.1021/ac00259a017.
- 34 S. Raiman, J. McMurray, R. Mayes, K. Myhre, J. Kurley, C. Abney, et al. "Holistic Approach to Understanding Alloy Degradation in Molten Chloride Salts." Abstracts of Papers of the American Chemical Society. American Chemical Society 2019.
- 35 K.G. Myhre, M.J. Mehta, M.Z. Martin, M. Du. "Laser Induced Breakdown Spectroscopy Analysis of Europium and Samarium in Aluminum Oxide". *Spectrochim. Acta Part B At. Spectrosc.* Elsevier, 2018. 149(June): 30–34. 10.1016/j.sab.2018.07.014.
- 36 D. Alamelu, A. Sarkar, S.K. Aggarwal. "Laser-induced Breakdown Spectroscopy for Simultaneous Determination of Sm, Eu and Gd in Aqueous Solution". *Talanta.* 2008. 77(1): 256–261. 10.1016/j.talanta.2008.06.021.
- 37 J. Serrano, L.M. Cabalín, J. Moros, J.J. Laserna. "Potential of Laser-induced Breakdown Spectroscopy for Discrimination of Nano-sized Carbon Materials. Insights on the Optical Characterization of Graphene". *Spectrochim. Acta Part B At. Spectrosc.* Elsevier B.V., 2014. 97: 105–112. 10.1016/j.sab.2014.05.003.
- 38 S. Grégoire, M. Boudinet, F. Pelascini, F. Surma, V. Detalle, Y. Holl. "Laser-induced Breakdown Spectroscopy for Polymer Identification". *Anal. Bioanal. Chem.* 2011. 400(10): 3331–3340. 10.1007/s00216-011-4898-2.
- 39 P. Pořízka, J. Klus, E. Képeš, D. Prochazka, D.W. Hahn, J. Kaiser. "On the Utilization of Principal Component Analysis in Laser-induced Breakdown Spectroscopy Data Analysis, A Review". *Spectrochim. Acta Part B At. Spectrosc.* Elsevier B.V., 2018. 148: 65–82. 10.1016/j.sab.2018.05.030.
- 40 D. Prochazka, M. Mazura, O. Samek, K. Rebrošová, P. Pořízka, J. Klus, et al. "Combination of Laser-induced Breakdown Spectroscopy and Raman Spectroscopy for Multivariate Classification of Bacteria". *Spectrochim. Acta Part B At. Spectrosc.* 2018. 139: 6–12. 10.1016/j.sab.2017.11.004.
- 41 A. Kramida, Y. Ralchenko, J. Reader, NIST ASD Team. NIST Atomic Spectra Database. Gaithersburg, MD, 2020. 10.18434/K5W30F.
- 42 M. Dong, L. Wei, J. Lu, W. Li, S. Lu, S. Li, et al. "A Comparative Model Combining Carbon Atomic and Molecular Emissions Based on Partial Least Squares and Support Vector Regression Correction for Carbon Analysis in Coal Using LIBS". *J. Anal. At. Spectrom.* Royal Society of Chemistry, 2019. 34(3): 480–488. 10.1039/C8JA00414E

Article

JAAS

1
2
3
4
5
6
7
8
9
10
11
12
13
14
15
16
17
18
19
20
21
22
23
24
25
26
27
28
29
30
31
32
33
34
35
36
37
38
39
40
41
42
43
44
45
46
47
48
49
50
51
52
53
54
55
56
57
58
59
60